

Article

Photonic Bandgaps of One-Dimensional Photonic Crystals Containing Anisotropic Chiral Metamaterials

Qian Wei [†], Jiaju Wu [†], Zhiwei Guo , Xiaotian Xu, Ke Xu, Yong Sun , Yunhui Li, Haitao Jiang ^{*} and Hong Chen

MOE Key Laboratory of Advanced Micro-Structured Materials, School of Physics Science and Engineering, Tongji University, Shanghai 200092, China; 2011297@tongji.edu.cn (Q.W.); wujiaju@tongji.edu.cn (J.W.); 2014guozhiwei@tongji.edu.cn (Z.G.); 1930957@tongji.edu.cn (X.X.); 2030950@tongji.edu.cn (K.X.); yongsun@tongji.edu.cn (Y.S.); liyunhui@tongji.edu.cn (Y.L.); hongchen@tongji.edu.cn (H.C.)

* Correspondence: jiang-haitao@tongji.edu.cn

[†] These authors contributed equally to this work.

Abstract: Conventional photonic bandgaps (PBGs) for linear polarization waves strongly depend on the incident angle. Usually, PBGs will shift toward short wavelengths (i.e., blue-shifted gaps) as the incident angle increases, which limits their applications. In some practices, the manipulation of PBGs for circular polarization waves is also important. Here, the manipulation of PBGs for circular polarization waves is theoretically investigated. We propose one-dimensional photonic crystals (1DPCs) containing anisotropic chiral metamaterials which exhibit hyperbolic dispersion for left circular polarization (LCP) wave and elliptical dispersion for right circular polarization (RCP) wave. Based on the phase variation compensation effect between anisotropic chiral metamaterials and dielectrics, we can design arbitrary PBGs including zero-shifted and red-shifted PBGs for LCP wave. However, the PBGs remain blue-shifted for RCP wave. Therefore, we can design a high-efficiency wide-angle polarization selector based on the chiral PBGs. Our work extends the manipulation of PBGs for circular polarization waves, which has a broad range of potential applications, including omnidirectional reflection, splitting wave and enhancing photonic spin Hall effect.

Keywords: photonic crystals; chiral photonic bandgaps; anisotropic chiral metamaterials; circular polarization waves



Citation: Wei, Q.; Wu, J.; Guo, Z.; Xu, X.; Xu, K.; Sun, Y.; Li, Y.; Jiang, H.; Chen, H. Photonic Bandgaps of One-Dimensional Photonic Crystals Containing Anisotropic Chiral Metamaterials. *Photonics* **2022**, *9*, 411. <https://doi.org/10.3390/photonics9060411>

Received: 23 April 2022

Accepted: 7 June 2022

Published: 10 June 2022

Publisher's Note: MDPI stays neutral with regard to jurisdictional claims in published maps and institutional affiliations.



Copyright: © 2022 by the authors. Licensee MDPI, Basel, Switzerland. This article is an open access article distributed under the terms and conditions of the Creative Commons Attribution (CC BY) license (<https://creativecommons.org/licenses/by/4.0/>).

1. Introduction

Photonic crystals (PCs) are artificial microstructures with periodic spatial modulation of electromagnetic parameters including permittivity, permeability or chiral parameter. The most typical characteristic of PCs is photonic bandgaps (PBGs) which forbid the propagation of electromagnetic waves within a given range of frequencies [1]. PBGs have attracted tremendous attention due to their many fascinating applications [2–5]. However, conventional all-dielectric photonic crystals have one shortcoming that the PBGs are angle-dependent. In some applications, zero-shifted PBGs, i.e., PBGs that will not shift as the incident angle changes, are needed. The emergence of metamaterials [6,7] or metasurfaces [8,9] has provided us with the possibility to design unconventional PBGs. In 2003, researchers realized zero-shifted PBGs in 1DPCs consisting of alternative dielectrics and negative-index metamaterials for linear polarization waves (transverse magnetic (TM) and transverse electric (TE) waves) [10,11]. The zero-shifted PBGs originate from an all-angle phase compensation effect between positive-index dielectric and negative-index metamaterial [11]. Nevertheless, it is a challenge to fabricate the negative-index metamaterials in the near-infrared or visible ranges.

On the other hand, another kind of artificial anisotropic material called hyperbolic metamaterial (HMM) has been intensively investigated [12–15]. HMMs possess a unique ability to manipulate light-matter interaction due to their special iso-frequency curves,

which can be utilized for spontaneous emission control [16,17], super-resolution imaging [18,19], sensing [20,21] and wavefront control [22,23]. Generally, HMMs can be mimicked by metal-dielectric multilayers with a subwavelength unit cell in the near-infrared or visible ranges [12,13]. Some natural materials also exhibit hyperbolic dispersion, such as hexagonal boron nitride (hBN) [24], α -phase molybdenum trioxide (α -MoO₃) [25], and other van der Waals materials [26,27]. Usually, HMMs can be classified into two types: a dielectric-type (Type I) HMM with $\epsilon_{\parallel} > 0$ and $\epsilon_{\perp} < 0$ and a metal-type (Type II) HMM with $\epsilon_{\parallel} < 0$ and $\epsilon_{\perp} > 0$ [12,14]. The dielectric-type HMM can also realize negative refraction [12]. Recently, based on the all-angle phase variation compensation effect, researchers have theoretically and experimentally realized zero-shifted PBGs in 1DPCs containing dielectric-type HMMs for TM waves [28,29]. The zero-shifted PBG can be utilized to design an omnidirectional reflector or absorber [30,31]. Later, researchers realized red-shifted PBGs (gap shifts toward long wavelength as the incident angle increases) in 1DPCs containing dielectric-type HMMs [32]. The red-shifted PBG can be used for biosensors [21] and polarization beam splitters for TM and TE waves [32].

The above works are restricted to the manipulation of PBGs for linear polarization waves. In some practices, the manipulation of PBGs for circular polarization waves is also important. In fact, it is possible to manipulate PBGs for circular polarization waves if we introduce chiral metamaterials into 1DPCs. Chiral materials possess the unique electromagnetic response known as optical activity. The chirality originates from the coupling between an electric field and magnetic field, and the electromagnetic coupling strength is denoted as κ . One can obtain the refractive index $\sqrt{\epsilon\mu} + \kappa$ for a right circular polarization (RCP) wave and the refractive index $\sqrt{\epsilon\mu} - \kappa$ for a left circular polarization (LCP) wave. As a result, chiral materials provide another way to achieve negative refraction in the case of $\kappa > \sqrt{\epsilon\mu}$ [33,34]. However, usually the chiral response is very weak for natural materials. Recently, researchers have used metamaterials or metasurfaces to enhance the chiral response [35], which greatly boosts chiro-optical activity [36,37] and circular dichroism [38–40]. The enhanced chirality is very useful in biological detection [41,42], sensing [43,44] and other applications [45,46]. It is expected that 1DPCs with chiral metamaterials would also control the propagation of light. In 2014, Cao et al. revealed blue-shifted chiral PBGs in 1DPCs containing negative-index chiral metamaterials [47]. Their work demonstrates the possibility for the manipulation of chiral PBGs (the PBGs are different for RCP and LCP waves, respectively) in 1DPCs.

In this paper, we propose another kind of 1DPCs containing anisotropic chiral metamaterials (ACMs). Besides blue-shifted chiral PBGs, we also obtain *zero-shifted* and *red-shifted* PBGs for the LCP wave, which will greatly extend the applications of chiral PBGs. Firstly, we introduce the chiral parameter κ into anisotropic media and realize the topological transition of dispersion for the LCP wave, in which the iso-frequency curves change from a closed ellipse to an open hyperbola [48–50]. Then, based on the phase variation compensation effect between ACMs and dielectrics [28,29,32], we design arbitrary chiral PBGs in 1DPCs. We obtain zero-shifted or red-shifted PBGs for the LCP wave and blue-shifted PBGs for the RCP wave. As a result, we can design a high-efficiency wide-angle polarization selector for circular polarization waves. Our work may facilitate the applications of splitting wave [32], omnidirectional reflection and absorption [30,31] and enhance the photonic spin Hall effect [51,52]. Finally, we draw our conclusions.

2. Theory Analysis

We considered 1DPCs composed of alternative ACMs and dielectrics, as shown in Figure 1. The whole structure is denoted by $(AB)_N$ where A and B represent the ACM and the dielectric with the thickness of d_A and d_B , respectively. The N represents the periodic number. The ACMs can be described by the constitutive relations [53]

$$\begin{aligned} \mathbf{D} &= \epsilon\mathbf{E} + i\kappa\mathbf{H} \\ \mathbf{B} &= \mu\mathbf{H} - i\kappa\mathbf{E} \end{aligned} \tag{1}$$

where $\epsilon = \text{diag}[\epsilon_x, \epsilon_y, \epsilon_z]$, $\mu = \text{diag}[\mu_x, \mu_y, \mu_z]$ and κ represents chiral parameter.

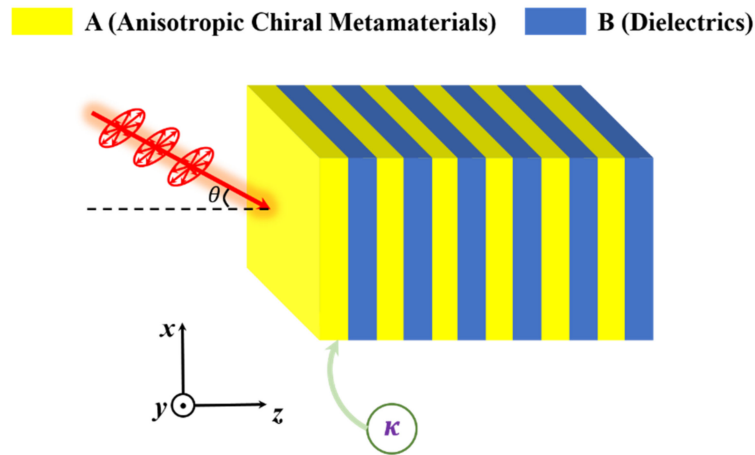


Figure 1. Schematic illustration of 1DPCs composed of ACMs and dielectrics. (A) and (B) represent an ACM and a dielectric, respectively.

The dispersion equation for ACMs and dielectrics can be expressed as [28,50]

$$\frac{k_x^2}{\rho_{\pm}} + k_{Az}^2 = k_t^2 \text{ and } k_x^2 + k_{Bz}^2 = \epsilon_B k_0^2 \tag{2}$$

where

$$\rho_{\pm} = \frac{1}{2} \left[\frac{\epsilon_{Az}}{\epsilon_{Ax}} + \frac{\mu_{Az}}{\mu_{Ax}} \pm \sqrt{\left(\frac{\epsilon_{Az}}{\epsilon_{Ax}} - \frac{\mu_{Az}}{\mu_{Ax}} \right)^2 + 4 \frac{\kappa^2}{\epsilon_{Ax} \mu_{Ax}}} \right] \text{ and } k_t^2 = \left(\frac{\omega}{c} \right)^2 \epsilon_{Ax} \mu_{Ax} \tag{3}$$

In Equation (2), ϵ_B denotes the permittivity of dielectric. In Equation (3), the “+” and “−” represent RCP and LCP waves, respectively. In practice, a dielectric slab with metallic inclusions [49,50,54] or metallic units [55] would mimic an ACM layer. If the metallic units are electric resonant units, the ACM will be nonmagnetic and $\mu_{Ax} = \mu_{Az} = 1$. The effective permittivity components and κ of ACM could be described as [55]

$$\begin{aligned} \epsilon_{Ax} &= \epsilon_b, \\ \epsilon_{Az} &= \epsilon_b - \frac{F_e \omega^2}{(\omega^2 - \omega_e^2 + i\gamma_e \omega)} \text{ and } \\ \kappa &= 1 - \frac{F_{\kappa} \omega^2}{(\omega^2 - \omega_{\kappa}^2 + i\gamma_{\kappa} \omega)} \end{aligned} \tag{4}$$

In Equation (4), we choose $\epsilon_b = 3$, $F_e = F_{\kappa} = 0.3$, $\omega_e = \omega_{\kappa} = 5 \times 10^{15}$ Hz, $\gamma_e = \gamma_{\kappa} = 6.2 \times 10^{13}$ Hz. Figure 2a,b give the real and imaginary parts of ϵ_{Az} and κ as a function of wavelength, respectively. In our paper, the dielectric is selected as silicon. In the wavelength range from 400 to 610 nm, the refractive index of silicon (denoted by n_{Si}) is also complex and dispersive. We use the refractive index of silicon from reference [56], which is shown in Figure 2c.

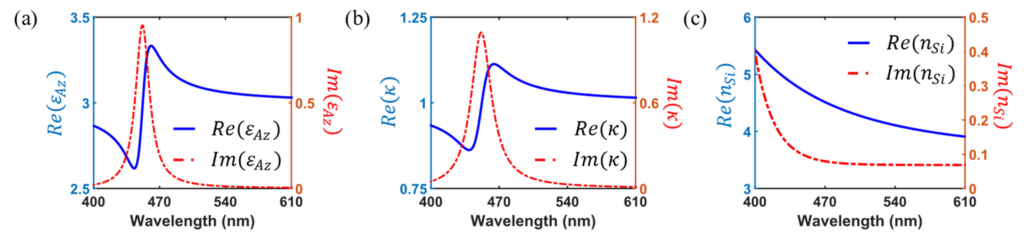


Figure 2. The real and imaginary parts of (a) ϵ_{Az} , (b) κ and (c) n_{Si} as a function of wavelength, respectively.

Next, we discussed the topological transition of iso-frequency curves by changing the value of κ . Usually, the iso-frequency curves of dielectrics are elliptical for RCP and LCP waves. However, according to Equations (2) and (3), we can obtain elliptical or hyperbolic iso-frequency curves for ACMs as $\rho_+ > 0$ or $\rho_- < 0$. We only consider the real part of the parameters for calculating the iso-frequency curves. In Figure 2a, at $\lambda = 532 \text{ nm}$, $\epsilon_{Ax} = 3$, $\epsilon_{Az} = 3.12$. At first, we suppose that $\kappa = 0.05$. In this case, the ρ_{\pm} are greater than zero. Therefore, the iso-frequency curves are elliptical for LCP and RCP waves, as shown in Figure 3a. The iso-frequency curves of RCP and LCP waves degenerate at $k_x = 0$ because ACMs are uniaxial [50]. Next, when we take the value of κ at $\lambda = 532 \text{ nm}$ from Figure 2b, i.e., $\kappa = 1.05$, the topological transition of iso-frequency curves occurs [48–50], where the iso-frequency curves change from closed ellipses to open hyperbolas for LCP wave. Thus, an opened hyperbolic iso-frequency curve can be obtained, while the iso-frequency curves remain elliptical for RCP wave, as illustrated in Figure 3b.

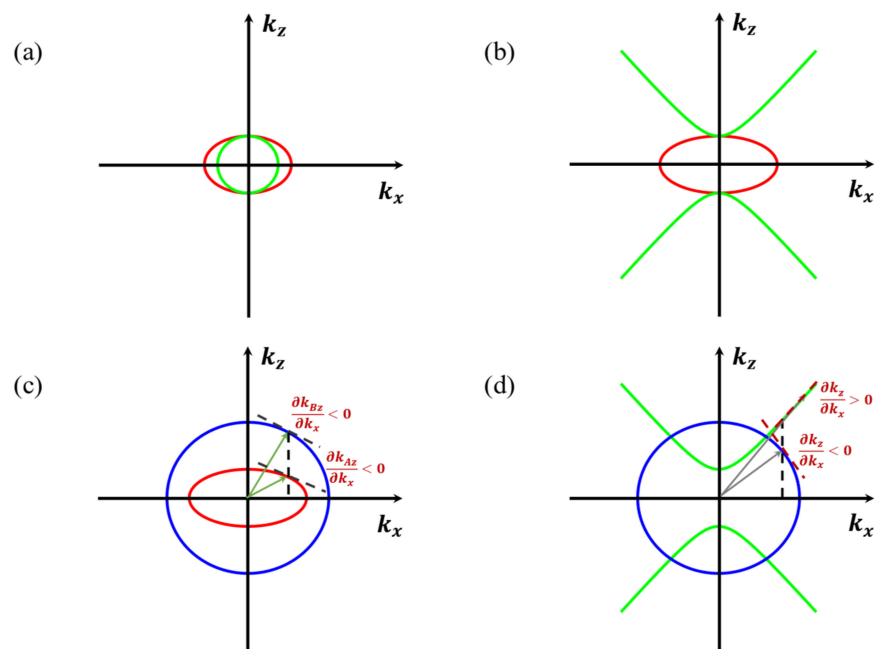


Figure 3. Iso-frequency curves of ACMs for RCP and LCP waves at (a) $\kappa = 0.05$ and (b) $\kappa = 1.05$. Iso-frequency curves of ACMs and silicon for (c) RCP and (d) LCP waves at $\lambda = 532 \text{ nm}$. The real part of the refractive index of silicon is 4.08, as taken from Figure 2c. Red and green solid lines represent the iso-frequency curves of ACMs for RCP and LCP waves, respectively. Blue solid line represents the iso-frequency curves of dielectrics for RCP and LCP waves.

Next, we consider the conditions for the manipulation of PBGs. The Bragg condition of the first PBG can be given by [10,28]

$$\Phi = (k_{Az}d_A + k_{Bz}d_B) \Big|_{\lambda_{Bragg}} = m\pi \tag{5}$$

where Φ represents the propagating phase within a unit cell, k_{Az} and k_{Bz} represent the wave vector along z direction in A and B layers, respectively. λ_{Bragg} represents the resonant wavelength within PBGs. Usually, the tangential wave vector component k_x will increase when the incident angle θ increases. As we can see from Figure 3c, both k_{Az} and k_{Bz} decrease when k_x increases. Therefore, to maintain the Bragg condition, the value of λ_{Bragg} will decrease as θ increases. This is the reason that the PBG shift towards short wavelength (i.e., blueshift) in all-dielectric 1DPCs. However, if we choose 1DPCs containing ACMs and dielectrics, the situation is different. From Figure 3d, we can see that k_{Az} increases as k_x increases within ACMs. As a comparison, k_{Bz} decreases as k_x increases within dielectrics. This means that Δk_z has different signs in the two materials. Therefore, the zero-shifted PBGs will occur if the phase variations between ACMs and dielectric can compensate each other ($\Delta k_{Az}d_A + \Delta k_{Bz}d_B = 0$) [28,29]. Similarly, if the phase variation in the ACM layer is larger than the absolute value of the phase variation in the dielectric layer, i.e., the over-compensated case that $\Delta k_{Az}d_A + \Delta k_{Bz}d_B > 0$, the red-shifted PBGs will occur [32]. One can easily find $\partial\Phi/\partial\theta = (\partial\Phi/\partial k_x) \cdot (\partial k_x/\partial\theta)$, where $\partial k_x/\partial\theta = k_0 \cos\theta > 0$. Therefore, we only consider the sign of $\partial\Phi/\partial k_x$ to obtain the condition of arbitrary chiral PBGs in 1DPCs. We further differentiate Equation (5) with respect to k_x and obtain

$$\frac{\partial\Phi}{\partial k_x} = \frac{\partial k_{Az}}{\partial k_x}d_A + \frac{\partial k_{Bz}}{\partial k_x}d_B \tag{6}$$

As shown in Figure 3c,d, one can see that the sign of $\partial k_{Az}/\partial k_x$ may be positive (LCP) or negative (RCP) in ACMs, while the sign of $\partial k_{Bz}/\partial k_x$ is still negative within dielectrics, regardless of the LCP or RCP waves. Therefore, we can arbitrarily tune the sign of $\partial\Phi/\partial k_x$. Remarkably, the sign of $\partial\Phi/\partial k_x$ is negative, zero and positive, corresponding to blue-shifted, zero-shifted and red-shifted PBGs, respectively. Next, based on $\partial\Phi/\partial k_x = 0$, we can obtain the thickness of A and B layers for zero-shifted condition (see Appendix A for detailed derivation), as follows

$$\begin{aligned} d_A &= -\frac{\pi c}{\omega_{Bragg} \epsilon_B k_0} \frac{\rho - k_t}{\sqrt{\epsilon_{Ax}\rho - k_t}} \text{ and} \\ d_B &= \frac{\pi c}{\omega_{Bragg} \epsilon_B k_0} \frac{\sqrt{\epsilon_B k_0}}{\sqrt{\epsilon_{Ax}\rho - k_t}} \end{aligned} \tag{7}$$

Furthermore, if $\partial\Phi/\partial k_x > 0$, we can obtain the thickness of A and B layers for redshifted condition, as follows

$$\begin{aligned} d'_A > d_A &= -\frac{\pi c}{\omega_{Bragg} \epsilon_B k_0} \frac{\rho - k_t}{\sqrt{\epsilon_{Ax}\rho - k_t}} \text{ and} \\ d_B &= \frac{\pi c}{\omega_{Bragg} \epsilon_B k_0} \frac{\sqrt{\epsilon_B k_0}}{\sqrt{\epsilon_{Ax}\rho - k_t}} \end{aligned} \tag{8}$$

3. Numerical Simulation and Applications

According to the above discussion, we firstly considered conventional PBGs of chiral 1DPC $(AB)_6$ for LCP and RCP waves. For the structural parameters, we set $d_A = 228$ nm, $d_B = 20$ nm and $\kappa = 0.05 + 0.01i$. We assumed that both the incident and exit media are air. On the basis of the anisotropic transfer matrix method (TMM) [57], we calculated the reflectance spectra as a function of wavelengths and incident angles for LCP and RCP waves, as shown in Figure 4a. We can see the PBG shifts toward the short wavelength as the incident angle increases, regardless of the LCP and RCP waves, which is similar to all-dielectric PCs for the TM and TE waves [2]. Next, we considered ACMs with κ shown in Figure 2b and other parameters remain unchanged, in which the iso-frequency curves are hyperbolas for the LCP wave while the iso-frequency curves of the RCP wave are elliptical. Similarly, the reflectance spectra of the LCP and RCP waves are shown in Figure 4b. For the LCP wave, $\lambda_{Bragg} = 532$ nm. As we can see, both gap edges only shift slightly at large

incident angles for the LCP wave, while those shift toward the short wavelength as the incident angle increases for the RCP wave, which agrees well with our theoretical analysis in Section 2. Therefore, we obtained the zero-shifted PBGs for the LCP wave. We further chose $d_A = 274$ nm and $d_B = 20$ nm based on Equation (8), and other parameters are the same as those used in Figure 4b. The reflectance spectra of the LCP and RCP waves are given in Figure 4c. Comparing the LCP wave with the RCP wave, we can see red-shifted gaps for the LCP wave while there are blue-shifted gaps for the RCP wave. To better demonstrate how the gap edges shift, we further extracted the wavelength of gap edges as a function of the incident angle for LCP and RCP waves from 0° to 90° , as shown in Figure 4d–f, respectively.

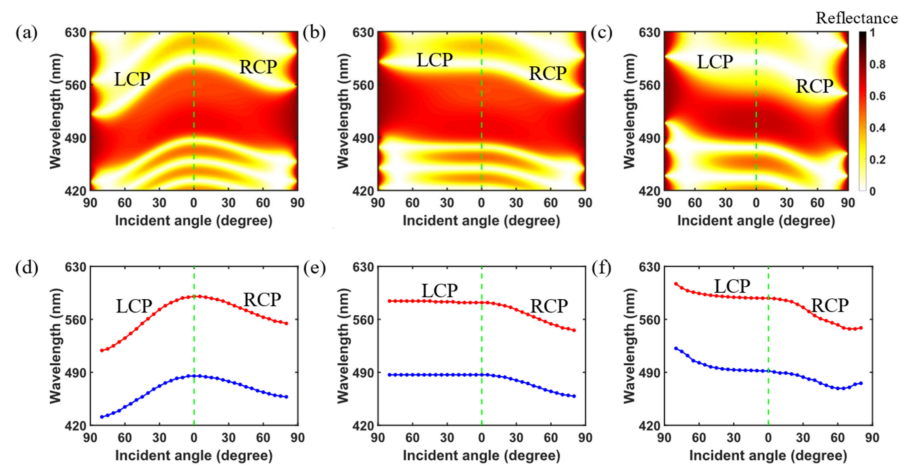


Figure 4. Reflectance spectra of $(AB)_6$ versus incident angles for LCP and RCP waves. (a) $d_A = 228$ nm, $d_B = 20$ nm and $\kappa = 0.05 + 0.01i$. (b) $d_A = 228$ nm, $d_B = 20$ nm and κ is taken from Figure 2b. (c) $d_A = 274$ nm, $d_B = 20$ nm and κ is taken from Figure 2b. (d–f) Gap edges corresponding to (a–c), respectively. The red (blue) solid line represents the upper (lower) band edge.

Based on the chiral PBGs (different PBGs for different circularly polarized waves) as shown in Figure 4c,f, we can design a wide-angle polarization selector for RCP and LCP waves. The reflectance of LCP and RCP waves at $\lambda = 514$ nm and $\lambda = 566$ nm, respectively, are shown in Figure 5a,b. We can clearly see that the reflectance always remains at a low value for the LCP wave at $\lambda = 514$ nm and RCP wave at $\lambda = 566$ nm, while it increases sharply for the RCP and LCP waves at the two wavelengths over a broad range of angles, which leads to a high polarization selection ratio at a wide-angle range. We define the $\rho_l = R^{RCP}/R^{LCP}$ and $\rho_u = R^{LCP}/R^{RCP}$ as the short-wavelength and long-wavelength polarization selection ratio, respectively. We consider that the angle range in which $\rho > 4$ is regarded as the efficient polarization selection for the structure. From Figure 5c,d, we can see a high polarization selection ratio at a wide-angle range from 19.6° to 66.8° at $\lambda = 514$ nm and from 20.7° to 64.2° at $\lambda = 566$ nm, respectively. Therefore, the structure can be utilized as a high-efficiency polarization selector for circular polarization waves. Interestingly, the chiral PBGs can also be utilized to enhance the photonic spin Hall effect [52,58], which refers to the phenomenon that the left and right-handed circularly polarized components split and produce transverse displacement when a Gaussian beam is reflected or transmitted at the interface of the structure. This photonic spin Hall effect can be expressed from the reflection coefficient ratio of LCP and RCP waves. The red-shifted PBG for the LCP wave and the blue-shifted PBG for the RCP wave can greatly enhance the reflectivity ratio between LCP and RCP waves. Therefore, the structure also facilitates the application of enhancing the photonic spin Hall effect.

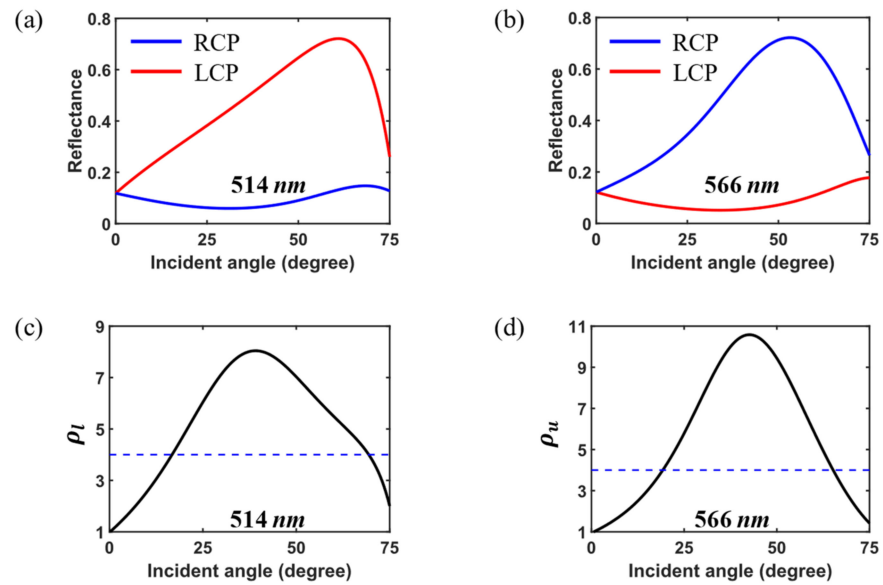


Figure 5. Reflectance for LCP and RCP waves at (a) $\lambda = 514$ nm and (b) $\lambda = 566$ nm, respectively. The blue (red) dotted line represents the reflectance of LCP (RCP) wave. Polarization selection ratio versus incident angles at (c) $\lambda = 514$ nm and (d) $\lambda = 566$ nm, respectively. The blue dashed lines indicate $\rho = 4$.

4. Conclusions

In summary, we theoretically studied the chiral PBGs in 1DPCs containing ACMs. The PBGs can be arbitrarily designed to be blue-shifted, zero-shifted or red-shifted. Particularly, our work provides a way to design a high-efficiency wide-angle polarization selector for circular polarization waves, owing to the fact that the gap edges are red-shifted for the LCP wave and blue-shifted for the RCP wave. The manipulation of chiral PBGs would also facilitate the applications of omnidirectional reflection and absorption, splitting wave and enhancing the photonic spin Hall effect for circularly polarized waves.

Author Contributions: Conceptualization, H.J.; methodology, Q.W. and J.W.; validation, H.C.; formal analysis, Q.W., J.W., Z.G., X.X., K.X., Y.S., Y.L., H.J. and H.C.; investigation, Q.W. and J.W.; resources, Q.W. and J.W.; data curation, Q.W. and J.W.; writing—original draft preparation, Q.W.; writing—review and editing, J.W. and H.J.; visualization, Q.W. and J.W.; supervision, H.J. and H.C.; project administration, Q.W. and J.W.; funding acquisition, H.J. All authors have read and agreed to the published version of the manuscript.

Funding: This work is sponsored by the National Key Research Program of China (Grant No. 2021YFA1400602) and the National Natural Science Foundation of China (Nos. 11774261, 12004284 and 61621001).

Institutional Review Board Statement: Not applicable.

Informed Consent Statement: Not applicable.

Data Availability Statement: Not applicable.

Conflicts of Interest: The authors declare no conflict of interest.

Appendix A

Here, we present a detailed derivation on two conditions for the zero-shifted and redshifted gaps. For LCP wave, we rewrite Equation (2) as $k_{Az} = k_t \sqrt{1 - k_x^2 / (\rho - k_t^2)}$ and $k_{Bz} = \sqrt{\epsilon_B k_0} \sqrt{1 - k_x^2 / (\epsilon_B k_0^2)}$. Under the conditions of $|\epsilon_{Az}| \gg 1$ and $\epsilon_B \gg 1$, k_{Az} and k_{Bz} can be Taylor expanded to the first-order series, as follows

$$k_{Az} \approx k_t \left(1 - \frac{k_x^2}{2k_t^2 \rho_-}\right) \text{ and} \tag{A1}$$

$$k_{Bz} \approx \sqrt{\epsilon_B} k_0 \left(1 - \frac{k_x^2}{2\epsilon_B k_0^2}\right)$$

Substituting Equation (A1) into Equation (5), we have

$$\frac{d_A}{d_B} = -\frac{\rho_- k_t}{\epsilon_B k_0} \tag{A2}$$

At normal incidence, the Bragg condition can be given by

$$\sqrt{\epsilon_{Ax}} d_A + \sqrt{\epsilon_B} d_B = \frac{\pi c}{\omega_{Brg}} \tag{A3}$$

Combining Equation (A2) with Equation (A3), we can obtain two conditions for the zero-shifted gaps

$$d_A = -\frac{\pi c}{\omega_{Brg}} \frac{\rho_- k_t}{\epsilon_B k_0 - \sqrt{\epsilon_{Ax}} \rho_- k_t} \text{ and} \tag{A4}$$

$$d_B = \frac{\pi c}{\omega_{Brg}} \frac{\sqrt{\epsilon_B} k_0}{\epsilon_B k_0 - \sqrt{\epsilon_{Ax}} \rho_- k_t}$$

Similarly, in the case of $\partial\Phi/\partial k_x > 0$, we can obtain two conditions for the redshift gaps

$$d'_A > d_A = -\frac{\pi c}{\omega_{Brg}} \frac{\rho_- k_t}{\epsilon_B k_0 - \sqrt{\epsilon_{Ax}} \rho_- k_t} \text{ and} \tag{A5}$$

$$d_B = \frac{\pi c}{\omega_{Brg}} \frac{\sqrt{\epsilon_B} k_0}{\epsilon_B k_0 - \sqrt{\epsilon_{Ax}} \rho_- k_t}$$

References

- Joannopoulos, J.D.; Johnson, S.G.; Winn, J.N.; Meade, R.D. *Molding the Flow of Light*, 4th ed.; Princeton University Press: Princeton, NJ, USA, 2008.
- Fink, Y.; Winn, J.N.; Fan, S.; Chen, C.; Michel, J.; Joannopoulos, J.D.; Thomas, E.L. A dielectric omnidirectional reflector. *Science* **1998**, *282*, 1679–1682. [[CrossRef](#)] [[PubMed](#)]
- Qiu, M.; Azizi, K.; Karlsson, A.; Swillo, M.; Jaskorzynska, B. Numerical studies of mode gaps and coupling efficiency for line-defect waveguides in two-dimensional photonic crystals. *Phys. Rev. B* **2011**, *64*, 155113. [[CrossRef](#)]
- Painter, O.; Lee, R.; Scherer, A.; Yariv, A.; O'Brien, J.; Dapkus, P.; Kim, I. Two-dimensional photonic band-gap defect mode laser. *Science* **1999**, *284*, 1819–1821. [[CrossRef](#)] [[PubMed](#)]
- Hu, X.; Jiang, P.; Ding, C.; Yang, H.; Gong, Q. Picosecond and low-power all-optical switching based on an organic photonic-bandgap microcavity. *Nat. Photonics* **2008**, *2*, 185–189. [[CrossRef](#)]
- Pendry, J.B. Negative refraction makes a perfect lens. *Phys. Rev. Lett.* **2000**, *85*, 3966. [[CrossRef](#)]
- Shelby, R.A.; Smith, D.R.; Schultz, S. Experimental verification of a negative index of refraction. *Science* **2001**, *292*, 77–79. [[CrossRef](#)]
- Ko, Y.H.; Razmjooei, N.; Hemmati, H.; Magnusson, R. Perfectly-reflecting guided-mode-resonant photonic lattices possessing Mie modal memory. *Opt. Express* **2021**, *29*, 26971–26982. [[CrossRef](#)]
- Razmjooei, N.; Ko, Y.H.; Simlan, F.A.; Magnusson, R. Resonant reflection by microsphere arrays with AR-quenched Mie scattering. *Opt. Express* **2021**, *29*, 19183–19192. [[CrossRef](#)]
- Li, J.; Zhou, L.; Chan, C.T.; Sheng, P. Photonic band gap from a stack of positive and negative index materials. *Phys. Rev. Lett.* **2003**, *90*, 083901. [[CrossRef](#)]
- Jiang, H.; Chen, H.; Li, H.; Zhang, Y.S.; Zhu, S. Omnidirectional gap and defect mode of one-dimensional photonic crystals containing negative-index materials. *Appl. Phys. Lett.* **2003**, *83*, 5386–5388. [[CrossRef](#)]
- Poddubny, A.; Iorsh, I.; Belov, P.; Kivshar, Y. Hyperbolic metamaterials. *Nat. Photonics* **2013**, *7*, 948–957. [[CrossRef](#)]
- Narimanov, E.E. Photonic hypercrystals. *Phys. Rev. X* **2014**, *4*, 041014. [[CrossRef](#)]
- Guo, Z.; Jiang, H.; Chen, H. Hyperbolic metamaterial: From dispersion manipulation to applications. *J. Appl. Phys.* **2020**, *127*, 071101. [[CrossRef](#)]
- Drachev, V.P.; Podolskiy, V.A.; Kildishev, A.V. Hyperbolic metamaterials: New physics behind a classical problem. *Opt. Express* **2013**, *21*, 15048–15064. [[CrossRef](#)]
- Lu, D.; Kan, J.J.; Fullerton, E.E.; Liu, Z. Enhancing spontaneous emission rates of molecules using nanopatterned multilayer hyperbolic metamaterials. *Nat. Nanotechnol.* **2014**, *9*, 48–53. [[CrossRef](#)]

17. Tumkur, T.; Zhu, G.; Black, P.; Barnakov, Y.A.; Bonner, C.E.; Noginov, M.A. Control of spontaneous emission in a volume of functionalized hyperbolic metamaterial. *Appl. Phys. Lett.* **2011**, *99*, 1115. [[CrossRef](#)]
18. Lu, D.; Liu, Z. Hyperlenses and metalenses for far-field super-resolution imaging. *Nat. Commun.* **2012**, *3*, 1–9. [[CrossRef](#)]
19. Guo, Z.; Jiang, H.; Zhu, K.; Sun, Y.; Li, Y.; Chen, H. Focusing and super-resolution with partial cloaking based on linear-crossing metamaterials. *Phys. Rev. Appl.* **2018**, *10*, 064048. [[CrossRef](#)]
20. Sreekanth, K.V.; Mahalakshmi, P.; Han, S.; Mani Rajan, M.S.; Choudhury, P.K.; Singh, R. Enhancing the angular sensitivity of plasmonic sensors using hyperbolic metamaterials. *Adv. Opt. Mater.* **2016**, *4*, 1767–1772. [[CrossRef](#)]
21. Wu, J.; Wu, F.; Xue, C.; Guo, Z.; Jiang, H.; Sun, Y.; Li, Y.; Chen, H. Wide-angle ultrasensitive biosensors based on edge states in heterostructures containing hyperbolic metamaterials. *Opt. Express* **2019**, *27*, 24835–24846. [[CrossRef](#)]
22. Yin, X.; Zhu, H.; Guo, H.; Deng, M.; Xu, T.; Gong, Z.; Li, X.; Hang, Z.; Wu, C.; Li, H.; et al. Hyperbolic metamaterial devices for wavefront manipulation. *Laser Photonics Rev.* **2019**, *13*, 1800081.
23. Gao, W.; Fang, F.; Liu, Y.; Zhang, S. Chiral surface waves supported by biaxial hyperbolic metamaterials. *Light Sci. Appl.* **2015**, *4*, e328. [[CrossRef](#)]
24. Caldwell, J.D.; Kretinin, A.V.; Chen, Y.; Giannini, V.; Fogler, M.M.; Francescato, Y.; Ellis, C.T.; Tischler, J.G.; Woods, C.R.; Giles, A.J.; et al. Sub-diffractive volume-confined polaritons in the natural hyperbolic material hexagonal boron nitride. *Nat. Commun.* **2014**, *5*, 1–9. [[CrossRef](#)]
25. Hu, G.; Ou, Q.; Si, G.; Wu, Y.; Wu, J.; Dai, Z.; Krasnok, A.; Mazon, Y.; Zhang, Q.; Bao, Q.; et al. Topological polaritons and photonic magic angles in twisted α -MoO₃ bilayers. *Nature* **2020**, *582*, 209–213. [[CrossRef](#)] [[PubMed](#)]
26. Geim, A.K.; Grigorieva, I.V. Van der Waals heterostructures. *Nature* **2013**, *499*, 419–425. [[CrossRef](#)]
27. Dorrell, W.; Pirie, H.; Gardezi, S.M.; Drucker, N.C.; Hoffman, J.E. Van der Waals metamaterials. *Phys. Rev. B* **2020**, *101*, 121103. [[CrossRef](#)]
28. Xue, C.; Ding, Y.; Jiang, H.; Li, Y.; Wang, Z.; Zhang, Y.; Chen, H. Dispersionless gaps and cavity modes in photonic crystals containing hyperbolic metamaterials. *Phys. Rev. B* **2016**, *93*, 125310. [[CrossRef](#)]
29. Wu, F.; Lu, G.; Xue, C.; Jiang, H.; Guo, Z.; Zheng, M.; Chen, C.; Du, G.; Chen, H. Experimental demonstration of angle-independent gaps in one-dimensional photonic crystals containing layered hyperbolic metamaterials and dielectrics at visible wavelengths. *Appl. Phys. Lett.* **2018**, *112*, 041902. [[CrossRef](#)]
30. Wu, F.; Guo, Z.; Wu, J.; Jiang, H.; Du, G. Band gap engineering and applications in compound periodic structure containing hyperbolic metamaterials. *Acta Phys. Sin.* **2020**, *69*, 154205. [[CrossRef](#)]
31. Wu, F.; Wu, X.; Xiao, S.; Liu, G.; Li, H. Broadband wide-angle multilayer absorber based on a broadband omnidirectional optical Tamm state. *Opt. Express* **2021**, *29*, 23976–23987. [[CrossRef](#)]
32. Wu, F.; Lu, G.; Guo, Z.; Jiang, H.; Xue, C.; Zheng, M.; Chen, C.; Du, G.; Chen, H. Redshift gaps in one-dimensional photonic crystals containing hyperbolic metamaterials. *Phys. Rev. Appl.* **2018**, *10*, 064022. [[CrossRef](#)]
33. Pendry, J.B. A chiral route to negative refraction. *Science* **2004**, *306*, 1353–1355. [[CrossRef](#)] [[PubMed](#)]
34. Wu, C.; Li, H.; Wei, Z.; Yu, X.; Chan, C.T. Theory and experimental realization of negative refraction in a metallic helix array. *Phys. Rev. Lett.* **2010**, *105*, 247401. [[CrossRef](#)] [[PubMed](#)]
35. Chen, Y.; Du, W.; Zhang, Q.; Ávalos-Ovando, O.; Wu, J.; Xu, Q.; Liu, N.; Okamoto, H.; Govorov, A.O.; Xiong, Q.; et al. Multidimensional nanoscopic chiroptics. *Nat. Rev. Phys.* **2021**, *4*, 113–124. [[CrossRef](#)]
36. Zhu, A.Y.; Chen, W.T.; Zaidi, A.; Huang, Y.W.; Khorasaninejad, M.; Sanjeev, V.; Qiu, C.W.; Capasso, F. Giant intrinsic chiro-optical activity in planar dielectric nanostructures. *Light Sci. Appl.* **2018**, *7*, 17158. [[CrossRef](#)]
37. Singh, R.; Plum, E.; Zhang, W.; Zheludev, N.I. Highly tunable optical activity in planar achiral terahertz metamaterials. *Opt. Express* **2010**, *18*, 13425–13430. [[CrossRef](#)]
38. Wang, Z.; Jia, H.; Yao, K.; Cai, W.; Chen, H.; Liu, Y. Circular dichroism metamirrors with near-perfect extinction. *ACS Photon.* **2016**, *3*, 2096–2101. [[CrossRef](#)]
39. Decker, M.; Klein, M.; Wegener, M.; Linden, S. Circular dichroism of planar chiral magnetic metamaterials. *Opt. Lett.* **2007**, *32*, 856–858. [[CrossRef](#)] [[PubMed](#)]
40. Wu, J.; Xu, X.; Su, X.; Zhao, S.; Wu, C.; Sun, Y.; Li, Y.; Wu, F.; Guo, Z.; Jiang, H.; et al. Observation of giant extrinsic chirality empowered by quasi-bound states in the continuum. *Phys. Rev. Appl.* **2021**, *16*, 064018. [[CrossRef](#)]
41. Hao, C.; Xu, L.; Kuang, H.; Xu, C. Artificial chiral probes and bioapplications. *Adv. Mater.* **2020**, *32*, 1802075. [[CrossRef](#)] [[PubMed](#)]
42. Manocchio, M.; Esposito, M.; Primiceri, E.; Leo, A.; Tasco, V.; Cuscuna, M.; Zuev, D.; Sun, Y.; Maruccio, G.; Romano, A.; et al. Femtomolar Biodetection by a Compact Core-Shell 3D Chiral Metamaterial. *Nano Lett.* **2021**, *21*, 6179–6187. [[CrossRef](#)] [[PubMed](#)]
43. Bakır, M.; Karaaslan, M.; Unal, E.; Karadag, F.; Alkurt, F.Ö.; Altıntaş, O.; Dalgac, S.; Sabah, C. Microfluidic and Fuel Adulteration Sensing by Using Chiral Metamaterial Sensor. *J. Electrochem. Soc.* **2018**, *165*, B475. [[CrossRef](#)]
44. Warning, L.A.; Miandashti, A.R.; McCarthy, L.A.; Zhang, Q.; Landes, C.F.; Link, S. Nanophotonic Approaches for Chirality Sensing. *ACS Nano* **2021**, *15*, 15538–15566. [[CrossRef](#)]
45. Ma, W.; Cheng, F.; Liu, Y. Deep-Learning-Enabled On-Demand Design of Chiral Metamaterials. *ACS Nano* **2018**, *12*, 6326. [[CrossRef](#)] [[PubMed](#)]
46. Wang, L.; Huang, X.; Li, M.; Dong, J. Chirality selective metamaterial absorber with dual bands. *Opt. Express* **2019**, *27*, 25983–25993. [[CrossRef](#)] [[PubMed](#)]

47. Cao, Y.; Li, J. Complete band gaps in one-dimensional photonic crystals with negative refraction arising from strong chirality. *Phys. Rev. B* **2014**, *89*, 115420. [[CrossRef](#)]
48. Krishnamoorthy, H.N.; Jacob, Z.; Narimanov, E.; Kretzschmar, I.; Menon, V.M. Topological transitions in metamaterials. *Science* **2012**, *336*, 205–209. [[CrossRef](#)]
49. Gao, W.; Lawrence, M.; Yang, B.; Liu, F.; Fang, F.; Beri, B.; Li, J.; Zhuang, S. Topological photonic phase in chiral hyperbolic metamaterials. *Phys. Rev. Lett.* **2015**, *114*, 037402. [[CrossRef](#)]
50. Cheng, Q.; Cui, T.J. Negative refractions in uniaxially anisotropic chiral media. *Phys. Rev. B* **2006**, *73*, 113104. [[CrossRef](#)]
51. Kapitanova, P.V.; Ginzburg, P.; Rodríguez-Fortuño, F.J.; Filonov, D.S.; Voroshilov, P.M.; Belov, P.A.; Poddubny, A.N.; Kivshar, Y.S.; Wurtz, G.A.; Zayats, A.V. Photonic spin Hall effect in hyperbolic metamaterials for polarization-controlled routing of subwavelength modes. *Nat. Commun.* **2014**, *5*, 1–8. [[CrossRef](#)]
52. Xia, J.; Chen, Y.; Xiang, Y. Enhanced spin Hall effect due to the redshift gaps of photonic hypercrystals. *Opt. Express* **2021**, *29*, 12160–12168. [[CrossRef](#)] [[PubMed](#)]
53. Lindell, I.V.; Sihvola, A.H.; Tretyakov, S.A.; Viitanen, A.J. *Electromagnetic Waves in Chiral and Bi-Isotropic Media*; Artech House: Norwood, MA, USA, 1994.
54. Xiao, M.; Lin, Q.; Fan, S. Hyperbolic Weyl point in reciprocal chiral metamaterials. *Phys. Rev. Lett.* **2016**, *117*, 057401. [[CrossRef](#)] [[PubMed](#)]
55. Chen, X.; Wu, B.; Kong, J.; Grzegorzczk, T.M. Retrieval of the effective constitutive parameters of bianisotropic metamaterials. *Phys. Rev. E* **2005**, *71*, 046610. [[CrossRef](#)] [[PubMed](#)]
56. Aspnes, D.E.; Studna, A.A.; Kinsbron, E. Dielectric properties of heavily doped crystalline and amorphous silicon from 1.5 to 6.0 eV. *Phys. Rev. B* **1984**, *29*, 768. [[CrossRef](#)]
57. Xiang, Y.; Dai, X.; Wen, S. Omnidirectional gaps of one-dimensional photonic crystals containing indefinite metamaterials. *J. Opt. Soc. Am. B* **2007**, *24*, 2033–2039. [[CrossRef](#)]
58. Xiang, Y.; Jiang, X.; You, Q.; Guo, J.; Dai, X. Enhanced spin Hall effect of reflected light with guided-wave surface plasmon resonance. *Photonics Rev.* **2017**, *5*, 467–472. [[CrossRef](#)]